RESEARCH ARTICLE | JULY 27 2018

Invited Article: Experimental evaluation of gold nanoparticles as infrared scatterers for advanced cardiovascular optical imaging Ⓕ

Special Collection: Biomedical Photonics

Jie Hu; Diego Romero Abujetas ⓘ ; Dionysia Tsoutsi ⓘ ; Luca Leggio; Fernando Rivero;
Emma Martín Rodríguez; Río Aguilar Torres; José A. Sánchez-Gil ⓘ ; Héctor Loro Ramírez; Daniel Gallego;
Horacio Lamela Rivera; Pilar Rivera Gil ⓘ ; Fernando Alfonso; José García Solé; Daniel Jaque

Check for updates

View Online   Export Citation   CrossMark

Invited Article: Experimental evaluation of gold nanoparticles as infrared scatterers for advanced cardiovascular optical imaging

Jie Hu,[1] Diego Romero Abujetas,[2] Dionysia Tsoutsi,[3] Luca Leggio,[4] Fernando Rivero,[5] Emma Martín Rodríguez,[6,7] Río Aguilar Torres,[5] José A. Sánchez-Gil,[2] Héctor Loro Ramírez,[8] Daniel Gallego,[4] Horacio Lamela Rivera,[4] Pilar Rivera Gil,[3] Fernando Alfonso,[5] José García Solé,[1] and Daniel Jaque[1,7,a]

[1]*Fluorescence Imaging Group, Departamento de Física de Materiales, Instituto Nicolás Cabrera, Facultad de Ciencias, Universidad Autónoma de Madrid, 28049 Madrid, Spain*
[2]*Instituto de Estructura de la Materia (IEM-CSIC), Consejo Superior de Investigaciones Científicas, Serrano 121, 28006 Madrid, Spain*
[3]*Integrative Biomedical Materials and Nanomedicine Lab, Department of Experimental and Health Sciences (DCEXS), Pompeu Fabra University (UPF), PRBB, Barcelona 08003, Spain*
[4]*Optoelectronics and Laser Technology Group (GOTL) Universidad Carlos III de Madrid, Avenida de la Universidad, 30, 28911 Leganés, Madrid, Spain*
[5]*Department of Cardiology, Hospital Universitario de la Princesa, Instituto Investigación Sanitaria Princesa (IIS-IP), Universidad Autónoma de Madrid, Calle Diego de León, 62, Madrid 28006, Spain*
[6]*Departamento de Física Aplicada, Facultad de Ciencias, Universidad Autónoma de Madrid, 28049 Madrid, Spain*
[7]*Instituto Ramón y Cajal de Investigación Sanitaria IRYCIS, Ctra. Colmenar Km. 9.100, Madrid 28034, Spain*
[8]*Facultad de Ciencias, Universidad Nacional de Ingeniería, P.O. Box 31-139, Lima, Peru*

The tremendous impact that cardiovascular diseases have in modern society is motivating the research of novel imaging techniques that would make possible early diagnosis and, therefore, efficient treatments. Cardiovascular optical coherence tomography (CV-OCT) emerged as a result of such a demand, and it has already been used at the clinical level. Full utilization of CV-OCT requires the development of novel contrast molecular agents characterized by a large scattering efficiency in the infrared (800-1400 nm). Gold nanoparticles (GNPs) seem to be the best candidates, but their scattering properties in the infrared are hardly known. In most of the cases, scattering properties are extracted from numerical simulations. This knowledge gap here is covered by providing an experimental evaluation of the infrared scattering properties of different GNPs (nanoshells, nanostars, and nanorods). These GNPs display remarkable extinction coefficients in the first and second biological windows, including the particular CV-OCT wavelength. We use a unique combination of techniques (thermal loading experiments, infrared optical coherence tomography, infrared dark field microscopy, and optoacoustic spectroscopy) to experimentally determine the scattering efficiency at three different near-infrared wavelengths (808 nm, 980 nm, and 1280 nm), lying in the first and second biological windows. Consequently, this work determines experimentally the influence of particle morphology on the infrared scattering efficiency of GNPs and evidences the existence of remarkable discrepancies between experimental data and numerical simulations. *© 2018 Author(s). All article content, except where otherwise noted, is licensed under a Creative Commons Attribution (CC BY) license (http://creativecommons.org/licenses/by/4.0/).* https://doi.org/10.1063/1.5027907

[a]Electronic mail: daniel.jaque@uam.es

3, 080803-1

I. INTRODUCTION

Cardiovascular diseases remain the main cause of mortality and morbidity in the western world. In addition to the primary prevention efforts, based on the establishment of healthy life habits, the fight against cardiovascular disorders requires the development of new diagnostic techniques. Of note, these diagnostic tools must increase the sensitivity and specificity, surpassing those that are already being applied at the clinical level. At the same time, new diagnostic techniques should minimize collateral effects. In this sense, cardiovascular optical imaging is gaining a considerable attention during the last decade as it could lead to a new generation of cost-effective and flexible diagnostic tools.[1–4] Intravascular imaging by intravascular ultrasound (IVUS), cardiovascular optical coherence tomography (CV-OCT), and the combination of IVUS and intravascular photoacoustic (IVPA) provide a detailed comprehensive visualization of coronary anatomy, overcoming many of the limitations of conventional angiography.[5] CV-OCT using near infrared light instead of sound pulses providing a high resolution of 15 μm for CV-OCT is compared to a resolution of 100 μm for IVUS and 35 μm for the IVUS/IVPA.[6–9] Currently, the main clinical use of CV-OCT is as a diagnostic tool to guide the optimization of percutaneous coronary interventions.[10,11] However, CV-OCT also encompasses different clinical scenarios, including assessing the natural history of atherosclerosis, providing unique information about the effects of different cardiovascular therapies, or unraveling the underlying mechanisms of acute coronary syndromes.[10,11]

Dual imaging systems based on the combination of CV-OCT and ultrasound imaging have already been developed for intravascular early detection of atherosclerosis.[12,13] As for most of the biomedical imaging techniques, cardiovascular optical imaging requires the use of near infrared light for clinical use. This light should lie in the first and second biological windows (I-BW and II-BW) that extend from 700 nm to 980 nm and from 1000 nm to 1400 nm, respectively, where tissues become partially transparent.[14] In fact, the machinery for clinical CV-OCT is based on a scanning laser operating at around 1.3 μm wavelength (II-BW). Clinical CV-OCT does not use contrast agents, and its performance is based on the detection of the contrast generated by tissue interfaces. In this way only, anatomic information of large areas is achieved, and early diagnosis is hampered. Early detection of atherosclerosis and other damages is crucial for an efficient treatment and survival rate enhancement. The use of infrared contrast agents enhances the spatial detection limits down to molecular levels, thus allowing early detection of damaged areas.[1,15,16]

Gold nanoparticles (GNPs) have shown to be excellent contrast agents for a variety of imaging techniques.[17,18] GNPs display a number of advantages for biomedical applications.[19] (i) They are inert, are biocompatible,[20] and can be properly functionalized with specific biological markers, allowing specific targeting and making possible the so-called "personalized diagnosis." (ii) GNPs can be easily synthesized by a variety of methods leading to different shapes (spheres, rod, cages, prisms, and stars) and sizes,[21–23] as well as combined core (dielectric)/shell (gold) spherically nanostructures, usually called gold nanoshells (GNSs). (iii) The morphology of GNPs determines the spectral position of their localized surface plasmon resonance (SPR, related to the collective oscillations of free electrons confined at the dimensions of such nanometric particles). By tuning GNP morphology, their optical response can be custom-made depending on the application.[24] Indeed, it is possible to shift the SPR of GNPs from the visible to the BWs, to enable *in vivo* applications. (iv) The scattering and absorption properties of GNPs can also be tuned depending on the selected NP's geometry.[25,26] Thus, these advantages enable the use of GNPs as photo-thermal transducers for in *in vivo* treatments, as contrast agents for optical imaging (multiphoton excited fluorescence imaging and scattering based imaging techniques), for optoacoustic (OA) imaging and for X-ray computer tomography.[14,18,27–31]

Because of the previously described advantages, GNPs constitute potential contrast agents for CV-OCT imaging, provided that their SPR is allocated in the II-BW. Indeed, recent studies have experimentally demonstrated this possibility by using both high aspect ratio gold nanorods (GNRs) and GNSs in combination with a clinical CV-OCT.[32] These results pointed out the great potential of GNPs with SPR in the II-BW for advanced CV imaging. The first step for the functional validation of these nanostructures as contrast agents for CV-OCT is a full understanding of their infrared optical properties, including the wavelength dependence of their absorption and scattering efficiencies. Such knowledge is imperative for CV-OCT image analysis, as well as to evaluate the thermal loading

during intravascular image acquisition. Until now, there are only few experimental studies dealing with the scattering/absorption efficiency of GNPs in the BWs. Indeed, most of the studies describing optical properties of GNPs are dealing with their response in the visible domain or in the I-BW.[33–35] The geometry dependence of the GNP scattering efficiency has been experimentally determined at 808 nm,[36] as this is the working wavelength of OCT systems for ophthalmology.[37,38] There are numerous predictive models on the optical response of different GNPs in the II-BW. However, an experimental validation of the wavelength dependence of both scattering and absorption efficiencies of GNPs in the BWs has not been demonstrated yet. Providing these experimental data is crucial for the functional validation of GNPs as contrast agents for advanced CV-OCT. In addition, it would help predict the optically induced heating of gold nanoparticles, which is of particular relevance to assess the intrinsic heating induced in optically trapped gold nanoparticles.[39]

In this work, we have experimentally determined the scattering and absorption efficiencies of different GNPs with their SPR extending (totally or partially) across the I and II-BWs. We have experimentally determined the scattering efficiency of three types of GNPs [gold nanorods, gold nanoshells, and gold nanostars (GNSTs)] displaying SPR with significant extinction at around 1.3 μm (the operating wavelength of the clinical CV-OCT apparatus). By means of a well-established photo-thermal method,[35,40,41] the wavelength dependence of the scattering efficiency has been elucidated by measuring it at 808 nm, 980 nm, and 1280 nm. Multi-wavelength experimental data have been compared with numerical simulations that failed to reproduce reliable values at long wavelengths. This fact stands out from the importance of an experimental determination of the scattering and absorption efficiencies. The scattering efficiency determined by the photo-thermal method has been corroborated by the combination of CV-OCT, infrared dark field microscopy (IR-DFM), and infrared OA spectroscopy (IR-OAS). The optimum GNP morphology for CV-OCT contrast enhancement has been determined, and the importance of the experimental determination of the spectral dependence of infrared scattering efficiency has been clearly evidenced.

II. EXPERIMENTAL SECTION

A. GNPs and TEM measurements

The GNRs, which are quasi-cylindrical nanoparticles, were purchased from Nanopartz, Inc. For extinction measurements, these nanoparticles [coated with polyethylene glycol (PEG) for water dispersibility] were diluted in 18 MEG de-ionized (DI) water, with a mass concentration of 0.05 mg/ml. Figure 1 shows representative transmission electron microscopy (TEM) images of these nanorods, showing a diameter of 11 ± 2 nm and a length of 90 ± 20 nm. GNSs were purchased
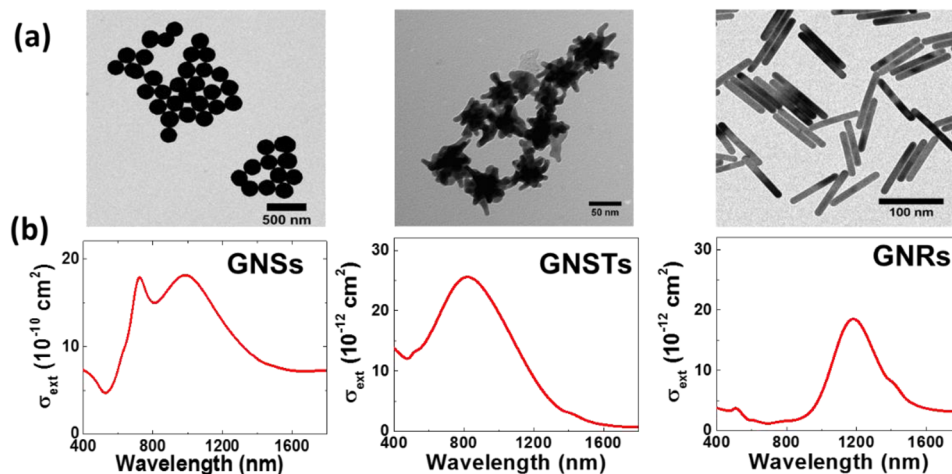

FIG. 1. (a) TEM images of the GNSs, GNSTs, and GNRs used along this work. (b) Extinction spectra obtained from colloidal suspensions of GNSs, GNSTs, and GNRs.

from nanoComposix. They consist in a dielectric (silica) core surrounded by a thin gold shell, having a core diameter of 16 nm and a total average diameter of 220 ± 23 nm (see the TEM image in Fig. 1 and size distribution in Fig. S1 of the supplementary material). These nanoparticles were coated with polyvinylpyrrolidone (PVP) (40 kDa) for water dispersibility. For extinction measurements, they were diluted in Milli-Q water, with mass concentration (0.053 mg/ml), i.e., similar to that used for GNRs. GNSTs (surfactant-free) were specifically synthesized for this work following a seed-mediated growth protocol, as previously reported by Yuan *et al.*[42] The following chemicals were used: Tetrachloroauric acid tetrahydrate ($HAuCl_4 \cdot 4H_2O$), trisodium citrate dihydrate ($C_6H_5O_7Na \cdot 2H_2O$), silver nitrate ($AgNO_3$), L(+)-ascorbic acid, and hydrochloric acid (HCl); all of them were purchased from Sigma-Aldrich and used without further purification. Water was purified using a Milli-Q system (Millipore). Aqua regia was used to clean all glassware prior to use. Gold spheres, used as seeds, were prepared by adding 15 ml of 1 wt. % citrate solution to a 100 ml boiling solution of $HAuCl_4$ (1 mM) under stirring and additional boiling for 15 min. This is a standard citrate-stabilized protocol producing wine-red colored gold sols with an average diameter of around 12 nm. Next, 1 ml of the above seed solution was added to a 100 ml of 0.25 mM $HAuCl_4$ solution containing 100 μl of 1M HCl at room temperature and under moderate stirring. Immediately afterwards, the addition of 1 ml of 3 mM $AgNO_3$ and 500 μl of 0.1M ascorbic acid was performed simultaneously and the solution was stirred for 30 s producing dark blue-black colloids. The nanostar dispersions were centrifuged at 4500 rpm for 20 min, redispersed in MiliQ-water, and kept in the dark at 4 °C for long-term storage. Figure 1 includes a TEM image obtained for these nanoparticles. They consist in solid gold nanospheres with an average diameter of 28 ± 4 nm together with different lobes (in average 14) with an average length of 14 ± 3 nm (see size distribution in Fig. S1 of the supplementary material).

B. Extinction experiments

The room-temperature extinction spectra of the GNPs were measured with an UV/VIS/near-infrared (NIR) spectrophotometer (Perkin Elmer Lambda1050).

C. Thermal loading experiments

For the determination of the absorption and scattering efficiencies, the heating and cooling cycles corresponding to a colloidal suspension of GNPs subjected to a modulated laser beam were recorded [see Fig. 2(b)]. The thermal images of the colloidal suspensions were acquired by using a thermographic camera (FLIR E40bx). The time-modulated lasers used were fiber coupled laser diodes operating at 808, 980, and 1280 nm.

D. Cardiovascular OCT experiments

A commercially available CV-OCT imaging system (Dragon-Fly™ OPTIS™; St. Jude Medical, St. Paul, MN, USA) available at the Interventional Cardiology Unit of the Hospital Universitario
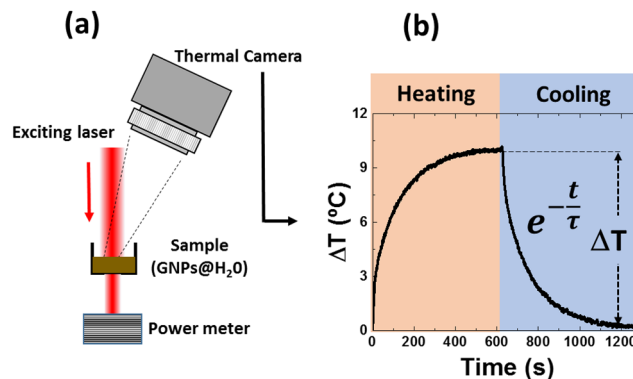

FIG. 2. (a) Schematic diagram of the experimental setup used for the determination of the scattering efficiency of GNPs under optical excitation in the II-BW. (b) Representative heating and cooling curve obtained from an aqueous solution of GNRs under 1280 nm optical excitation.

La Princesa (Madrid, Spain) was used. More details about the OCT system could be found in our previous papers.[32,43] The OCT catheter was inserted in a tube (3-mm inner diameter) into which different solutions of GNPs were injected separately for measuring their OCT signal.

E. Optoacoustic experiment

The optoacoustic signals were obtained by using a fiber-coupled Nd:YAG laser operating at 1064 nm and providing 8 ns width pulses as the excitation source. The laser had a repetition rate of 1 kHz and a pulse energy of 10.5 μJ, leading to an average power of 10.5 mW. The GNPs were placed in a cuvette with a thickness of 4 mm. In order to perform comparable measurements, the concentration of GNPs in the solutions was adjusted to provide an optical density (OD) of 10 at the laser wavelength (1064 nm). The optoacoustic signals generated in the sample were detected by an ultrasound transducer mechanically attached to the cuvette. The signal generated by the ultrasound transducer was sent to a 40 dB pre-amplifier and collected by a digital oscilloscope.[44]

F. Infrared dark field microscopy

A conventional optical microscope equipped with a dark-field condenser (NA 0.80–0.95) was used. The forward scattering image was collected by using a 50× microscope objective with a numerical aperture of 0.35. Illumination was performed employing a broadband white source. The dark field images were taken by using a XEVA-320 infrared camera. This camera is based on an InGaAs 2D array cooled down to 0 °C that makes the detection of fluorescence images in the 900–1700 nm spectral range possible. A combination of infrared long-pass filters was placed at the entrance of the infrared camera so that the only scattered radiation with the wavelength at 1300 ± 50 nm was recorded.

III. RESULTS AND DISCUSSION

A. Infrared extinction cross section of GNPs

Three different types of GNPs were investigated in this work: GNRs, GNSs, and gold nanostars (GNSTs), respectively. The transmission electron microscopy (TEM) images of the investigated structures have been included in Fig. 1(a). The average dimensions of each structure, as obtained from the statistical analysis of TEM images, are given in the supplementary material (Fig. S1). These were selected due to the combination of shape and size that produces high extinction cross section in the BWs. Figure 1 includes the extinction cross-sectional spectra of these three structures. In the case of GNRs, the extinction coefficients peak is around 1200 nm (longitudinal surface plasmon) that extend from about 900 nm to about 1600 nm, including the relevant infrared wavelengths that were investigated in this work; 808 nm, 980 nm, and 1280 nm (the CV-OCT working wavelength). For the case of GNSs, the extinction spectrum is constituted by a very broadband that results from the spectral overlap between two bands at 730 nm and 1040 nm. GNSs display the broadest extinction spectrum (from about 600 nm to about 1600 nm) while providing the largest extinction cross section values (about two orders of magnitude larger than those of GNRs and GNSTs). In particular, their high extinction cross section at 1280 nm (1.1×10^{-9} cm^2) makes them particularly suitable for CV-OCT.[32] Finally, the extinction cross section of GNSTs is constituted by a plasmonic band peaking at about 800 nm that extends in the IR spectral region from about 500 nm to about 1600 nm. Such SPRs are electric dipole resonances stemming from the collective oscillations of Au electrons. As such, they are sensitive to nanoparticle shape (except for very small nanoparticle), especially along the direction of electric field polarization of the incident light. Thus GNRs exhibit two plasmonic bands, the longer (respectively, shorter) wavelength peak corresponding to the longitudinal (respectively, transverse) SPR;[21,22] note in Fig. 1(b) that the transverse SPR is much weaker than the longitudinal one, as expected. On the other hand, plasmonic bands for GNSs are polarization-independent due to their spherical symmetry; in this case, the shorter-wavelength plasmonic band arises from a quadrupolar SPR.[45] GNSTs are not spherically symmetric; however, for a sufficiently large number of star tips pointing to all directions, they are nearly polarization independent.[42,46,47] The position and strength of the SPR can be in principle controlled by either NP parameters or interparticle distances, although

in a complex manner. The influence of each NP separately is as expected; the larger and sharper the GNSTs are, the stronger and more redshifted the resulting SPR is.[41] Aggregation makes it more complicated: for a simple dimer, it is nonetheless well known that the shorter the interparticle distance, the stronger and more redshifted the resulting SPR.[48]

B. Experimental determination of infrared scattering efficiency

The determination of the wavelength dependence of the infrared scattering efficiency (η_s) is based on the experimental determination of the photo-thermal heating conversion efficiency (η_h). η_h is defined as the fraction of extinct (scattered or absorbed) energy by a single nanoparticle that is converted into heat. For non-luminescent nanoparticles, as it is our case, all absorbed energy by a single nanoparticle is converted into heat so that the photo-thermal conversion efficiency is equal to the absorption efficiency (η_a) (i.e., $\eta_h = \eta_a$). Hereafter, the scattering/absorption efficiency is defined as the fraction of extinct light by a nanoparticle that is scattered/absorbed. At a given wavelength (λ), it can be written as

$$\eta_h(\lambda) = \eta_a(\lambda) = \frac{\sigma_{abs}(\lambda)}{\sigma_{abs}(\lambda) + \sigma_{sct}(\lambda)} = \frac{\sigma_{abs}(\lambda)}{\sigma_{ext}(\lambda)}, \tag{1}$$

where $\sigma_{abs}(\lambda)$, $\sigma_{sct}(\lambda)$, and $\sigma_{ext}(\lambda)$ are the absorption, scattering, and extinction cross sections at a wavelength λ, respectively. If the photo-thermal conversion efficiency η_h is known, then the scattering efficiency can be calculated straightforwardly since $\eta_s + \eta_a = 1$, and thus

$$\eta_s(\lambda) = 1 - \eta_a(\lambda) = 1 - \eta_h(\lambda). \tag{2}$$

The photo-thermal conversion efficiency can be evaluated by measuring the input/output heat balance under transient illumination, as previously reported.[35,40,49] Figure 2(a) shows the experimental arrangement used all along this work to measure $\eta_h(\lambda)$. The method is described in detail in the supplementary material. It is based on the measurement of the heating and cooling curve of a solution containing the GNPs when it is optically excited by a fiber coupled laser diode. A representative heating/cooling curve is shown in Fig. 2(b). From this curve, it is possible to estimate the absorption efficiency, which is given by

$$\eta_a = 1 - \eta_s = \frac{\frac{mC_p\Delta T_{max}}{\tau} - Q_r}{P_0\left(1 - 10^{-OD}\right)}, \tag{3}$$

where m, C_p, and OD are the mass, specific heat, and optical density of the solution containing the GNPs. P_0 is the incident laser power, ΔT_{max} is the maximum temperature increment [indicated in Fig. 2(b)], and τ is the relaxation time of the cooling process [also indicated in Fig. 2(b)]. Equation (3) gives the photo-thermal efficiency (equal to the absorption efficiency) from parameters that are either known or can be experimentally measured. For instance, the specific data shown in Fig. 2(b) correspond to the heating and cooling cycles of an aqueous solution of GNRs excited at 1280 nm and for the particular values $m = 0.5$ g, $P_0 = 160$ mW, $OD = 1.075$, $\Delta T_{max} = 9.92\,°C$, and $\tau = 104.3$ s. Substituting these values in Eq. (3), we obtain an absorption efficiency of 0.95 and, therefore, a scattering efficiency of 0.05. In order to obtain an accurate statistical value of the scattering efficiency, we carried out experiments at different input powers for each one of the three illumination wavelengths investigated here (see Table S1 in the supplementary material). Note that once the scattering efficiency at a given wavelength (λ) is experimentally determined it is possible to get the scattering extinction cross section at this wavelength since

$$\sigma_{sct}(\lambda) = \eta_{sct}(\lambda) \cdot \sigma_{ext}(\lambda), \tag{4}$$

where $\sigma_{ext}(\lambda)$ is the extinction cross section at wavelength λ as experimentally determined from the extinction spectra included in Fig. 1. In Table I, we have listed the averaged scattering efficiencies, extinction cross sections, and scattering cross sections, as obtained for each GNP at the three wavelengths. Fast inspection of Table I reveals that the largest scattering efficiencies and cross sections are provided by GNSs. Actually, the scattering efficiency of GNSs is higher than 50%, for the three wavelengths investigated in this work. Consequently, these results indicate that GNSs are the most suitable nanoparticles for scattering based imaging techniques, such as OCT and optical microscopy.[50,51]

TABLE I. Experimentally determined scattering efficiencies and scattering cross sections at three wavelengths investigated.

	808 nm			980 nm			1280 nm		
	η_{sct}	σ_{ext} (cm^2)	σ_{sct} (cm^2)	η_{sct}	σ_{ext} (cm^2)	σ_{sct} (cm^2)	η_{sct}	σ_{ext} (cm^2)	σ_{sct} (cm^2)
GNSs	0.68	1.50×10^{-9}	1.02×10^{-9}	0.84	1.81×10^{-9}	1.52×10^{-9}	0.51	1.09×10^{-9}	5.56×10^{-10}
GNRs	0.05	1.64×10^{-12}	0.82×10^{-13}	0.23	5.00×10^{-12}	1.15×10^{-12}	0.12	1.42×10^{-11}	1.70×10^{-12}
GNSTs	0.10	2.55×10^{-11}	2.55×10^{-12}	0.16	2.06×10^{-11}	3.30×10^{-12}	0.44	5.59×10^{-12}	2.46×10^{-12}

Data included in Table I also reveal that the scattering efficiency is strongly wavelength dependent for both GNSs and GNSTs. Although GNSTs show very low scattering efficiencies at 800 and 980 nm, they present a scattering efficiency close to 50% at around 1.3 μm.

C. Numerical calculations and comparison with experimental data

In order to provide theoretical insight into the measured extinction spectra and the experimentally determined scattering efficiencies for the different GNPs, we have made use of full electrodynamic methods to calculate the spectral dependence of the extinction, absorption, and scattering cross sections. For GNSs, calculations were carried out by using the discrete-dipole-approximation method, in particular, the open-source Fortran-90 software package discrete dipole scattering (DDSCAT).[52] For more complex shapes, such as GNRs and GNSTs, numerical calculations were carried out by means of a free software implementation, called SCUFF[53] (open-source software package for analysis of electromagnetic scattering problems using the method of moments). Gold permittivity data were obtained from Johnson and Christy measurements,[54] and we assumed that the medium permittivity is that of water (n = 1.33). Thus, GNRs were considered as cylinders with a given length and radius and with endcaps terminated as hemispheres with the same radius. At the same time, GNSs, with a simple geometry, were considered as a spherical core (made of silica) homogeneously covered by a spherical protective shell made of gold.

For the case of GNSTs, the situation is more complex and a crucial issue is how to define the nanostar geometry. In this regard, we defined a nanostar shape inspired by our TEM images (Fig. 1). Rather than exploiting analytical formulation (as in Ref. 46, which poses some difficulties in the meshing procedure), we assumed that the nanostars contain a spherical core, with fourteen elongated tips with semi-ellipsoidal shape [see Fig. S2(a) of the supplementary material]. Due to the structural inhomogeneities shown in the TEM images of the GNTSs, we fixed the spherical core radius as R = 15 nm and the tip ellipsoidal cross section (along two short axes) as a circle with radius r = 5 nm. The tip length L (long axis of the ellipsoid) is then allowed to vary between 12 and 25 nm [which nearly corresponds to the tip length and angle (θ = atan(r/L)], as observed in the TEM images. The resulting calculated cross-sectional spectra are shown in Fig. S2(b) of the supplementary material for monochromatic plane waves with varying vacuum wavelength impinging onto the nanostars along the x direction with linear polarization along the vertical axis (with respect to the nanostar shown in the inset). Strong SPRs appear with narrow width in the range 700-950 nm, with a ratio between absorption and extinction of ~87%. In this regard, it should be emphasized that, despite the anisotropic shape of the nanostars, the resulting spectra are nearly isotropic and polarization independent, as we have verified (though not shown) by varying the angle of incidence and the electric field polarization. Actually, this was also pointed out in Ref. 47 even for smoother nanostars with fewer tips. The reason is that the SPR, being essentially a dipolar resonance, is excited mostly at any angle of incidence due to the fact that the electric field vector stretches along the direction between any of the opposing nanostar tips, whose length (~2R + 2L) in turn controls the SPR wavelength. As a matter of fact, upon the increase in the nanostar tip length, the SPR is red-shifted, covering the spectral range between 700 and 950 nm, consistently with the broad SPR width experimentally measured (see Fig. 1). To shed light on such inhomogeneous broadening, we carried out a smoothed weighted average over all spectra different tip lengths, assigning approximate weighs according to the statistics of GNST shapes. The resulting simulated spectra have been included in Fig. S2(b) of the supplementary material.

The numerically calculated extinction, absorption, and scattering cross-sectional spectra in the BWs are included in Fig. S3 of the supplementary material as calculated for GNSs, GNRs, and GNSTs.

By comparing these data with the experimentally obtained extinction spectra (see Fig. 1), we realize that while for GNSs there is a good agreement, the spectral shapes are not properly reproduced neither for GNRs nor for GNSTs. For GNRs, the calculated extinction cross-sectional spectrum (peaking at about 1300 nm) appears shifted to longer wavelengths in respect to the experimental one (peaking at about 1200 nm). In addition, the calculated spectrum is narrower than the experimental one. For GNSTs, while the peak position is certainly reproduced, the calculated spectrum appears much narrower than the experimental one, thus leading to a large inaccuracy when determining the cross section values and the scattering efficiencies at long wavelengths. This experimental broadening is likely due to the non-uniform nanostar geometries (e.g., wide distribution of the aspect ratio), as well as the finite-size effects, which broaden and dampen the resonance but do not influence the plasmon band position.[42] It should be borne in mind that this experimental broadening has also been reported elsewhere in connection with star-shaped nanoparticles[42] as stemming from both the nonuniform nanostar geometries and finite-size effects at the tip edges (shorter electron scattering mean free path). The former mechanism has been somehow taken into account through the average over GNST shapes inspired by the TEM images above, although larger shape variations and/or aggregation (not evidenced in the TEM images) might be responsible for the discrepancies. In addition, the other mechanism mentioned earlier, finite-size effects, also typically broadens resonance; it is due to the increased electron damping resulting from electron scattering at the narrow tips, similar to what occurs within GNS thin shells.[45,55]

By using the calculations included in Fig. S3 of the supplementary material, the wavelength dependence of scattering efficiency can also be numerically calculated for all investigated GNPs. Results of these calculations are included in Fig. 3 together with the experimental data. According to these numerical calculations, the scattering efficiency is weakly dependent on the wavelength for GNRs and GNSTs but strongly wavelength dependent for GNSs. While a good agreement between numerical simulations and measured efficiencies occurs at 800 nm and 980 nm, a clear disagreement is observed at around 1.3 μm (the CV-OCT wavelength) for GNSTs. At this specific wavelength, calculations predict a scattering efficiency of 0.09, much lower than that experimentally measured (0.44). While the origin of this discrepancy is not fully understood, the physical phenomenon behind this is the same that leads to the appearance of the long wavelength tail in the extinction spectrum. We state that the existence of interaction between individual GNSTs via agglomeration or slight contact between tips could lead to dimer structures with completely different optical properties. In particular, we state that the presence of such interacting structures could lead to red-shifts in the plasmon resonance and to larger scattering efficiencies. Regardless of the origin of these discrepancies, these highlight the importance of performing direct experimental measurements for the scattering efficiency at different wavelengths, as we did in this work.

D. Infrared scattering experiments

To gain insight into the actual scattering efficiency of GNPs at long wavelengths, where the calculated and measured data display the largest discrepancy, we carried out two sets of imaging measurement. In particular, we investigated the infrared scattering abilities of the three types of GNPs by IR-DFM and by CV-OCT. The results obtained in each case are described in the following.
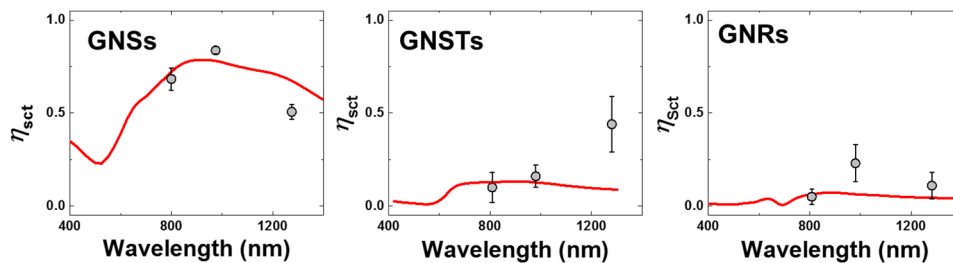

FIG. 3. Wavelength dependence of scattering efficiency of GNSs, GNSTs, and GNRs. Solid lines show results extracted from calculations, whereas dots correspond to the experimental data obtained in this work (see Table I).

1. Infrared dark field microscopy (IR-DFM)

For IR-DFM experiments, the GNPs were deposited and dried on microscope slides. The microscope slides containing the GNPs were visualized by using the home-made IR-DFM described in Sec. II, schematically drawn in Fig. S4 of the supplementary material. The IR-DFM system employed here is able to visualize individual GNPs by using their scattering abilities at 1300 ± 50 nm. Figure 4(a) shows the IR-DFM images obtained for the three GNPs studied in this work. Up to the best of our knowledge, these are the first ever reported IR-DFM images of GNPs in the II-BW. As can be observed, all GNPs can be detected by IR-DFM, revealing a non-vanishing scattering cross section in the three cases (in accordance with the experimental data included in Fig. 3). The largest IR-DFM contrast is provided by GNSs, being significantly larger than that provided by GNSTs and GNRs. This is evidenced in Fig. 4(b), in which we have included the average IR-DFM intensity per spot as generated by GNSs, GNRs, and GNSTs. The results included in Fig. 4 are, therefore, in qualitative agreement with the experimentally and calculated values of the scattering cross sections (see Table I). These experimental data confirm that GNSs provide the largest infrared scattering cross section among the geometries studied here.

2. Cardiovascular optical coherence tomography

The infrared scattering ability of the different GNPs at around 1.3 μm has also been investigated by performing CV-OCT experiments. In this case, we injected colloidal solution of each type of GNP (GNSs: 0.053 mg/ml, GNRs: 0.05 mg/ml, GNSTs: 0.043 mg/ml) into a tubing (see Fig. S5 of the supplementary material). Once the aqueous solutions of GNPs were inside the tubing (mimicking an artery), the CV-OCT catheter was introduced into the tubing, allowing for the detection of the individual GNPs by means of their back-scattering efficiency.[32] It should be noted that the advantage of this interferometric technique is that it provides an indirect measure of the infrared back-scattering cross section at the single wavelength of 1.3 μm. Figure 5(a) shows the CV-OCT cross-sectional images for the colloidal solutions containing the three investigated GNPs. Again, the three geometries studied here produced a significant CV-OCT signal. This again reveals a non-vanishing infrared scattering cross section at around 1.3 μm. It is also evident from Fig. 5(a) that the CV-OCT contrast is provided by each type of GNP. The integrated intensities corresponding to these cross-sectional images are shown in Fig. S6 of the supplementary material. From these results, we obtained the OCT intensity per NP for each type of GNPs, as shown in Fig. 5(b).
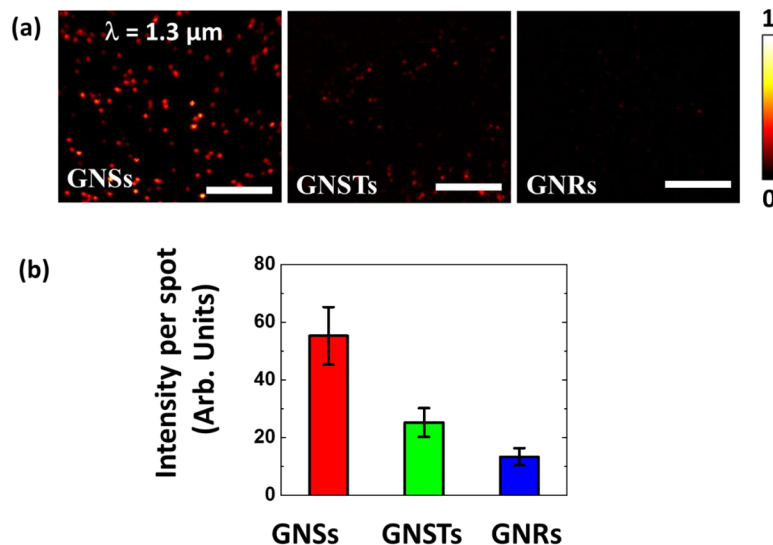
FIG. 4. (a) Infrared dark field images obtained at 1.3 μm by using GNSs, GNRs, and GNSTs as potential contrast agents. The scale bar is 20 μm in all cases. (b) Average intensity per nanoparticle generated by GNSs, GNRs, and GNSTs as obtained from the statistical analysis of images included in the left column.
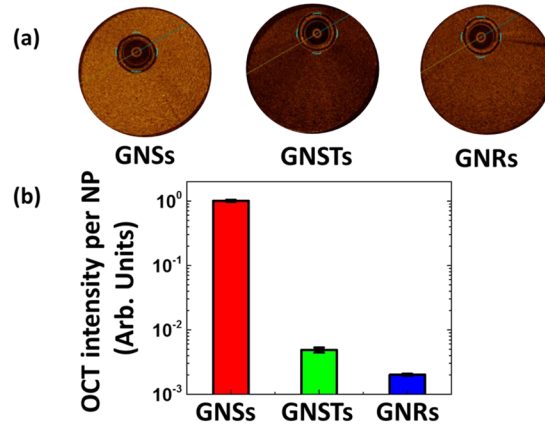
FIG. 5. (a) OCT cross-sectional images of colloidal solutions containing GNSs, GNSTs, and GNR. (b) OCT intensities of single GNSs, GNSTs, and GNRs obtained from the statistical analysis of figures included in the left column.

Again, it is found that the largest contrast is provided by GNSs, revealing their superior scattering cross section.

We can now discuss on the concordance between the experimental data included in Fig. 5 and Table I. For a sample of thickness d containing a certain concentration of GNPs, i.e., N, the Lambert-Beer extinction law gives the fraction of scattered intensity,

$$\frac{I_0 - I}{I_0} = 1 - e^{-\sigma_{sct}Nd}, \tag{5}$$

where I_0 is the incident light intensity and I is the light intensity transmitted through the sample. For low values of the exponential exponent and assuming the same thickness for all measurements (same geometrical conditions), Eq. (5) can be written as

$$\frac{I_0 - I}{I_0} \approx \sigma_{sct}Nd. \tag{6}$$

Thus, the OCT intensities (per GNP) given in Fig. 5(b) should be proportional to the fraction of scattered light and so to experimental values of σ_{sct} (indeed to the backscattering cross section) given in Table I. Now, we can compare the OCT intensity per GNP ($I_{oct,}$) of each type of GNP normalized to that given by the GNSs (the best scatters). From the data given in Fig. 5, we obtain

$$I_{oct}(GNSTs)\Big/I_{oct}(GNSs) = 5 \times 10^{-3} \tag{7}$$

and

$$I_{oct}(GNRs)\Big/I_{oct}(GNSs) = 2 \times 10^{-3}. \tag{8}$$

Indeed, these values are close to the ratio between the scattering cross sections experimentally obtained and listed in Table I that leads to $\sigma_{sct}(GNRs)/\sigma_{sct}(GNSs) \approx 3.05 \times 10^{-3}$ and $\sigma_{sct}(GNSTs)/\sigma_{sct}(GNSs) \approx 4.42 \times 10^{-3}$. In fact, the slight discrepancy could be due to the different geometries that lead to different backscattering/scattering ratios. At this point, we conclude that the CV-OCT experimental results confirm the validity of the scattering efficiencies (and so the scattering cross sections) experimentally determined in this work by the photo-thermal method. In fact, the results reported here highlight the need for a direct determination of the scattering efficiency, particularly at longer wavelengths (as for the OCT wavelength), where numerical calculations for GNRs and GNSTs fail to explain the experimentally obtained extinction cross sections (see Figs. 1 and S3 of the supplementary material) and therefore to provide a reliable value for the scattering efficiency.
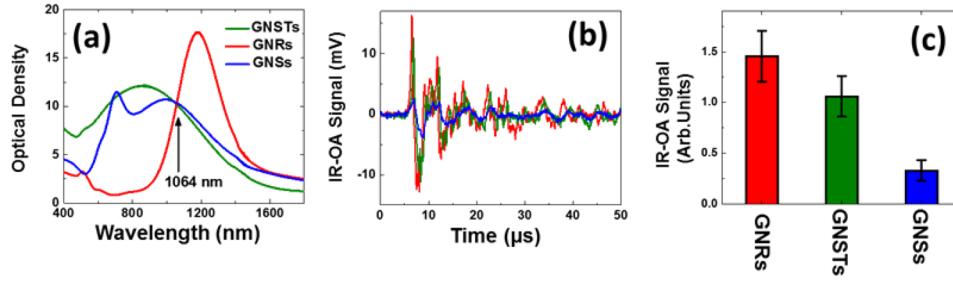
FIG. 6. (a) Optical density of GNRs (red), GNSTs (green), and GNSs (blue). (b) Time evolution of the IR-OA signals generated by the three GNPs after laser excitation. (c) Average IR-OA amplitudes obtained for the three GNPs.

3. Optoacoustic experiments

An indirect estimation of the geometry dependence of the scattering efficiency of GNPs can also be obtained by the performance of infrared-excited optoacoustic experiments (IR-OA).[56] For this purpose, we prepared colloidal solutions containing the three types of GNPs with exactly the same OD at 1064 nm (this being the wavelength used in our IR-OA experiments), as shown in Fig. 6(a). Each solution was introduced in a quartz cuvette mechanically attached to a piezo transducer connected to a signal amplifier and to a digital oscilloscope. In the absence of any fluorescence (as in our case), the magnitude of the IR-OA signal is proportional to the fraction of the absorbed pump power ($P_{abs} = P_0 \cdot (1 - 10^{-OD})$, where P_0 is the incident pump power) that is converted into heat. In other words, the IR-OA signal is expected to be proportional to $\eta_{abs} \cdot P_{abs}$. Therefore, we can write

$$I_{OA} = k \cdot (1 - \eta_{sct}) \cdot P_0 \cdot \left(1 - 10^{-OD}\right), \tag{9}$$

where k is a coupling constant that depends on the Grüneisen parameter and experimental conditions such as the gain of the piezo transducer. From Eq. (9), it is clear that the IR-OA signal is proportional to $(1 - \eta_{sct})$ in such a way that those GNPs with largest scattering efficiencies should give the lowest IR-OA signal with the same OD. Figure 6(b) shows the IR-OA signals generated by the three GNPs studied in this work. The three geometries generate measurable IR-OA signals, even though with quite different amplitudes. The averaged IR-OA amplitudes obtained for the three cases are displayed in Fig. 6(c). In this case, the lowest IR-OA signal was generated by the GNSs. This is in close agreement with the experimental data displayed in Fig. 3 and with Eq. (9) that predicts the lowest IR-OA for the GNPs with the largest scattering efficiency. The data included in Fig. 6(c) allow for a quantitative estimation of the relation between the infrared scattering efficiencies of the different GNPs studied in this work. Equation (9) can be rewritten to get a formal expression for the OA intensity ratio between GNSTs and GNSs so that

$$R_{OA}\left(\frac{GNSTs}{GNSs}\right) = \frac{I_{OA}(GNSTs)}{I_{OA}(GNSs)} = \frac{1 - \eta_{sct}(GNSTs)}{1 - \eta_{sct}(GNSs)}. \tag{10}$$

Analogously, we can write Eq. (10) as follows:

$$R_{OA}\left(\frac{GNRs}{GNSs}\right) = \frac{I_{OA}(GNRs)}{I_{OA}(GNSs)} = \frac{1 - \eta_{sct}(GNRs)}{1 - \eta_{sct}(GNSs)}. \tag{11}$$

From the experimental IR-OA data, we obtain $R_{OA}\left(\frac{GNSTs}{GNSs}\right) \approx R_{OA}\left(\frac{GNRs}{GNSs}\right) \approx 6$. From the numerically calculated scattering efficiencies (Table I), we obtain $R_{OA}\left(\frac{GNSTs}{GNSs}\right) \approx R_{OA}\left(\frac{GNRs}{GNSs}\right) \approx 4$. Therefore, it is found that the infrared scattering efficiencies determined by the numerical calculations explain well the infrared optoacoustic generation efficiency of the GNPs studied in this work.

IV. CONCLUSIONS AND FUTURE PERSPECTIVES

We have experimentally determined the infrared scattering efficiency and scattering cross section of GNPs with three different geometries: nanorods, nanoshells, and nanostars. Multi-wavelength

thermal loading experiments have been carried out to experimentally determine the spectral dependence of the scattering efficiency of these three nanoparticles. Comparison between experimental data and numerical simulation reveals good agreement in all three cases, except for GNSTs that present an unexpected large scattering efficiency at long wavelengths. These discrepancies have been explained in terms of size inhomogeneities as well due to particle-particle interactions. Both GNSs and GNSTs show that scattering efficiencies are strongly wavelength dependent, thus evidencing the importance of considering the spectral operating range when choosing the appropriate geometry for each particular imaging application. It is also experimentally found that, in the whole infrared spectral range investigated here (800-1400 nm), GNSs show the largest scattering efficiency and cross section. This explains their best performance as cardiovascular imaging probes, as concluded in previous studies.

The superior performance of GNSs as scattering units in the infrared has been confirmed by means of infrared dark field imaging, optical coherence tomography, and optoacoustic experiments. In all cases, the experimental data confirm the conclusions extracted from photo-thermal experiments and reveal the multifunctional character of these GNPs that are capable of efficient scattering and acoustic generation under infrared optical excitation.

It is important to stand out that the GNSs used here have a significantly larger size than the investigated GNRs and GNSs. This is otherwise required for displaying a significant surface plasmon resonance in the near infrared. This size difference should partially explain the dominant scattering efficiency of GNSs. In fact, Jain *et al.*[22] performed a systematic investigation of how the geometry and size of GNSs and GNRs affect their spectral properties by means of numerical simulations. They concluded that GNSs must be much larger than GNRs in order to tune its SPR to the near infrared. They also proposed that, for a given core/total ratio (0.85), the scattering efficiency of GNSs should decrease when reducing the total nanoshell radius. Indeed, it should be very interesting to test this prediction by direct measurements of the scattering efficiency, as we have made in this work.

In summary, the results shown in this work constitute the first experimental study of the infrared scattering properties of plasmonic nanoparticles and are the first step toward a complete understanding of their infrared optical properties. This is, in turn, essential if they have to be used as cardiovascular contrast agents providing unequivocal information. Nevertheless, the high sensitivity of CV-OCT, which has been proved to detect even small (about 5 nm) quantum dots,[57] indicates that by using this novel technique a large variety of scattering particles would be still useful as cardiovascular contrast agents.

SUPPLEMENTARY MATERIAL

See supplementary material for more details on the thermal loading experiments, characterization of GNPs, and simulations.

ACKNOWLEDGMENTS

[1] H. G. Bezerra, M. A. Costa, G. Guagliumi, A. M. Rollins, and D. I. Simon, JACC: Cardiovasc. Interventions **2**(11), 1035–1046 (2009).
[2] J. E. Phipps, T. Hoyt, T. E. Milner, and M. D. Feldman, Curr. Cardiovasc. Imaging Rep. **8**(8), 30 (2015).
[3] Z. A. Ali, K. K. Galougahi, A. Maehara, R. A. Shlofmitz, O. Ben-Yehuda, G. S. Mintz, and G. W. Stone, JACC: Cardiovasc. Interventions **10**(24), 2473–2487 (2017).
[4] F. Alfonso and F. Prati, Eur. Heart J. **38**(42), 3148–3151 (2017).

[5] C. V. Bourantas, F. A. Jaffer, F. J. Gijsen, G. van Soest, S. P. Madden, B. K. Courtney, A. M. Fard, E. Tenekecioglu, Y. Zeng, and A. F. van der Steen, Eur. Heart J. **38**(6), 400–412 (2016).

[6] N. Mamdani, B. Tung, Y. Wang, F. A. Jaffer, and A. Tawakol, Curr. Cardiovasc. Imaging Rep. **10**(7), 24 (2017).

[7] J.-C. Tardif, F. Lesage, F. Harel, P. Romeo, and J. Pressacco, Circ.: Cardiovasc. Interventions **4**(3), 319–333 (2011).

[8] X. Li, W. Wei, Q. Zhou, K. K. Shung, and Z. Chen, J. Biomed. Opt. **17**(10), 106005 (2012).

[9] A. G. Podoleanu, J. Microsc. **247**(3), 209–219 (2012).

[10] H. C. Lowe, J. Narula, J. G. Fujimoto, and I.-K. Jang, JACC: Cardiovasc. Interventions **4**(12), 1257–1270 (2011).

[11] F. Prati, E. Regar, G. S. Mintz, E. Arbustini, C. Di Mario, I.-K. Jang, T. Akasaka, M. Costa, G. Guagliumi, and E. Grube, Eur. Heart J. **31**(4), 401–415 (2009).

[12] X. Guo, D. P. Giddens, D. Molony, C. Yang, H. Samady, J. Zheng, G. S. Mintz, A. Maehara, L. Wang, and X. Pei, J. Biomech. Eng. **140**(4), 041005 (2018).

[13] S. D. Matthews and W. H. Frishman, Cardiol. Rev. **25**(2), 68–76 (2017).

[14] D. Jaque, L. M. Maestro, B. Del Rosal, P. Haro-Gonzalez, A. Benayas, J. Plaza, E. M. Rodriguez, and J. G. Sole, Nanoscale **6**(16), 9494–9530 (2014).

[15] F. A. Jaffer, P. Libby, and R. Weissleder, J. Am. Coll. Cardiol. **47**(7), 1328–1338 (2006).

[16] J. Zhang, Y. Zu, C. S. Dhanasekara, J. Li, D. Wu, Z. Fan, and S. Wang, Wiley Interdiscip. Rev.: Nanomed. Nanobiotechnol. **9**(1), e1412 (2017).

[17] E. C. Dreaden, A. M. Alkilany, X. Huang, C. J. Murphy, and M. A. El-Sayed, Chem. Soc. Rev. **41**(7), 2740–2779 (2012).

[18] M. Varna, H. V. Xuan, and E. Fort, Wiley Interdiscip. Rev.: Nanomed. Nanobiotechnol. **10**(1), e1470 (2018).

[19] J. Pérez-Juste, I. Pastoriza-Santos, L. M. Liz-Marzán, and P. Mulvaney, Coord. Chem. Rev. **249**(17-18), 1870–1901 (2005).

[20] K. Van Hoecke, K. De Schamphelaere, Z. Ali, F. Zhang, A. Elsaesser, P. Rivera-Gil, W. Parak, G. Smagghe, C. Howard, and C. Janssen, Nanotoxicology **7**(1), 37–47 (2013).

[21] K. M. Mayer and J. H. Hafner, Chem. Rev. **111**(6), 3828–3857 (2011).

[22] P. K. Jain, K. S. Lee, I. H. El-Sayed, and M. A. El-Sayed, J. Phys. Chem. B **110**(14), 7238–7248 (2006).

[23] P. Rivera_Gil, C. Vazquez-Vazquez, V. Giannini, M. P. Callao, W. J. Parak, M. A. Correa-Duarte, and R. A. Alvarez-Puebla, Angew. Chem., Int. Ed. **52**(51), 13694–13698 (2013).

[24] L. Dykman and N. Khlebtsov, Chem. Soc. Rev. **41**(6), 2256–2282 (2012).

[25] P. Zamora-Perez, D. Tsoutsi, R. Xu, and P. Rivera_Gil, Materials **11**(2), 243 (2018).

[26] D. Tsoutsi, M. Sanles-Sobrido, A. Cabo, and P. Rivera Gil, Curr. Med. Chem. **25**, 1–15 (2018).

[27] V. Amendola, R. Pilot, M. Frasconi, O. M. Maragò, and M. A. Iatì, J. Phys.: Condens. Matter **29**(20), 203002 (2017).

[28] W. Li and X. Chen, Nanomedicine **10**(2), 299–320 (2015).

[29] J. Hainfeld, D. Slatkin, T. Focella, and H. Smilowitz, Br. J. Radiol. **79**(939), 248–253 (2006).

[30] D. Kim, S. Park, J. H. Lee, Y. Y. Jeong, and S. Jon, J. Am. Chem. Soc. **129**(24), 7661–7665 (2007).

[31] P. Chhour, P. C. Naha, S. M. O'Neill, H. I. Litt, M. P. Reilly, V. A. Ferrari, and D. P. Cormode, Biomaterials **87**, 93–103 (2016).

[32] J. Hu, F. Rivero, R. A. Torres, H. Loro Ramírez, E. M. Rodríguez, F. Alfonso, J. García Solé, and D. Jaque, J. Biophotonics **10**(5), 674–682 (2017).

[33] Y. Liu, J. R. Ashton, E. J. Moding, H. Yuan, J. K. Register, A. M. Fales, J. Choi, M. J. Whitley, X. Zhao, and Y. Qi, Theranostics **5**(9), 946–960 (2015).

[34] F.-Y. Cheng, C.-T. Chen, and C.-S. Yeh, Nanotechnology **20**(42), 425104 (2009).

[35] H. Chen, L. Shao, T. Ming, Z. Sun, C. Zhao, B. Yang, and J. Wang, Small **6**(20), 2272–2280 (2010).

[36] V. P. Pattani and J. W. Tunnell, Lasers Surg. Med. **44**(8), 675–684 (2012).

[37] M. Wojtkowski, A. Kowalczyk, R. Leitgeb, and A. Fercher, Opt. Lett. **27**(16), 1415–1417 (2002).

[38] W. Drexler and J. G. Fujimoto, Prog. Retinal Eye Res. **27**(1), 45–88 (2008).

[39] A. Andres-Arroyo, F. Wang, W. J. Toe, and P. Reece, Biomed. Opt. Express **6**(9), 3646–3654 (2015).

[40] D. K. Roper, W. Ahn, and M. Hoepfner, J. Phys. Chem. C **111**(9), 3636–3641 (2007).

[41] J. R. Cole, N. A. Mirin, M. W. Knight, G. P. Goodrich, and N. J. Halas, J. Phys. Chem. C **113**(28), 12090–12094 (2009).

[42] H. Yuan, C. G. Khoury, H. Hwang, C. M. Wilson, G. A. Grant, and T. Vo-Dinh, Nanotechnology **23**(7), 075102 (2012).

[43] J. Hu, F. Sanz-Rodríguez, F. Rivero, E. M. Rodríguez, R. A. Torres, D. H. Ortgies, J. G. Solé, F. Alfonso, and D. Jaque, Nano Res. **11**(2), 676–685 (2018).

[44] L. Leggio, D. Gallego, R. Arroyo, S. B. Gawali, S. Rodriguez, M. Sánchez, G. Carpintero del Barrio, and H. Lamela, Prog. Electromagn. Res. **78**, 143–154 (2017).

[45] S. L. Westcott, J. B. Jackson, C. Radloff, and N. J. Halas, Phys. Rev. B **66**(15), 155431 (2002).

[46] R. Rodríguez-Oliveros and J. A. Sánchez-Gil, Opt. Express **20**(1), 621–626 (2012).

[47] R. Rodríguez-Oliveros, R. Paniagua-Domínguez, J. A. Sánchez-Gil, and D. Macías, Nanospectroscopy **1**(1), 67–96 (2015).

[48] O. Muskens, V. Giannini, J. Sánchez-Gil, and J. G. Rivas, Opt. Express **15**(26), 17736–17746 (2007).

[49] L. Marciniak, A. Pilch, S. Arabasz, D. Jin, and A. Bednarkiewicz, Nanoscale **9**(24), 8288–8297 (2017).

[50] J. A. Izatt, M. A. Choma, and A.-H. Dhalla, in *Optical Coherence Tomography: Technology and Applications*, edited by W. Drexler and J. G. Fujimoto (Springer, Cham, 2015), pp. 65–94.

[51] M. Hu, C. Novo, A. Funston, H. Wang, H. Staleva, S. Zou, P. Mulvaney, Y. Xia, and G. V. Hartland, J. Mater. Chem. **18**(17), 1949–1960 (2008).

[52] B. T. Draine and P. J. Flatau, J. Opt. Soc. Am. A **11**(4), 1491–1499 (1994).

[53] M. H. Reid and S. G. Johnson, IEEE Trans. Antennas Propag. **63**(8), 3588–3598 (2015).

[54] C. Ungureanu, R. R. Gopal, T. van Leeuwen, and S. Manohar, Phys. Rev. B **6**(12), 4370–4379 (1972).

[55] E. Prodan, P. Nordlander, and N. Halas, Nano Lett. **3**(10), 1411–1415 (2003).

[56] V. B. Cunningham, H. Lamela, and D. C. Gallego, J. Nanophotonics **7**(1), 073078 (2013).

[57] J. Hu, D. H. Ortgies, R. A. Torres, N. Fernández, L. Porto, E. M. Rodríguez, J. G. Solé, D. Jaque, F. Alfonso, and F. Rivero, Adv. Funct. Mater. **27**(41), 1703276 (2017).